PCCP

Accepted Manuscript

ROYAL SOCIETY OF CHEMISTRY

www.rsc.org/pccp

Magnetism in Olivine-type $LiCo_{1-x}Fe_xPO_4$ Cathode Materials: Bridging Theory and Experiment

Vijay Singh,[§] Yelena Gershinsky, [§] Monica Kosa, Mudit Dixit, David Zitoun,* Dan Thomas Major*

Department of Chemistry and the Lise Meitner-Minerva Center of Computational Quantum Chemistry and the Institute for Nanotechnology and Advanced Materials, Bar-Ilan University,
Ramat-Gan 52900, Israel

[§] Equal contribution

[*] Electronic mail: majort@biu.ac.il, david.zitoun@biu.ac.il

Abstract

In the current paper, we present a non-aqueous sol-gel synthesis of olivine type $LiCo_{1-x}Fe_xPO_4$ compounds (x = 0.00, 0.25, 0.50, 0.75, 1.00). The magnetic properties of the olivines are measured experimentally and calculated using first-principles theory. Specifically, the electronic and magnetic properties are studied in detail with standard density functional theory (DFT), as well as by including spin-orbit coupling (SOC), which couples the spin to the crystal structure. We find that the Co^{2+} ions exhibit strong orbital moment in the pure $LiCoPO_4$ system, which is partially quenched upon substitution of Co^{2+} by Fe^{2+}. Interestingly, we also observe a non-negligible orbital moment on the Fe^{2+} ion. We underscore that the inclusion of SOC in the calculations is essential to obtain qualitative agreement with the observed effective magnetic moments. Additionally, Wannier functions were used to understand the experimentally observed rising trend in the Néel temperature, which is directly related to the magnetic exchange interaction paths in the materials. We suggest that out of layer M – O – P – O – M magnetic interactions ($J_\perp$) are present in the studied materials. The current findings shed light on important differences observed in the electrochemistry of the cathode material $LiCoPO_4$ compared to the already mature olivine material $LiFePO_4$.

(1) Introduction

Current research in the field of lithium-ion batteries (LIBs) is focused on improving safety, cost, energy density and power density.[1-7] One of the possible avenues to increase the energy density of LIBs is employing high-voltage cathode materials. The $LiCoPO_4$ (LCP) olivine-type compound is a promising high-voltage cathode material due to its elevated working potential (4.8V vs Li/Li^+). In contrast, the commercially available iso-structured $LiFePO_4$ (LFP) olivine-type compound has a much lower working potential (3.7V vs Li/Li^+).[8, 9] Despite LCP′s advantageous working potential relative to LFP, its practical energy density and longevity is much poorer than expected, suggesting differences in the electronic and surface properties of the two olivine materials.[10]

Recently, mixed transition-metal olivine systems, i.e. $LiM_{1-z}M'_zPO_4$ (M, M' = divalent transition metals), have attracted considerable interest. These composite materials facilitate fine-tuning of the inherent properties of the pure analogues, such as voltage, conductivity and stability of the cathode upon delithiation.[11-13] Among these materials, the $LiCo_{1-y}Fe_yPO_4$[13-19] solid solution systems have drawn much attention, as these systems exhibit higher energy density and improved redox kinetics due to higher electronic conductivity in comparison to the pure olivines. $LiCo_{1-y}Fe_yPO_4$[13, 20, 21] and $LiCo_{1-y}Mn_yPO_4$[13, 22, 23] solid solutions are also appealing due to their high operating voltage arising from the Co^{2+}/Co^{3+} redox couple. Systematic studies of the physical and electrochemical properties of $Li_xM_{1-y}M'_yPO_4$ (M/M′ = Co and Mn and Fe) using experimental tools and density functional theory (DFT) calculations have appeared in the recent literature.[20,24, 25] The local environments in $LiCo_{1-x}Fe_xPO4$ were also characterized by Strobridge et al. using a combined NMR and first principles study.[26]

Recently, Kosova et al. studied the electrochemical performance of $LiCo_{1-y}Fe_yPO_4$ ($0 \leq y \leq 1$).[12] These authors showed that due to a shift of the Co^{2+}/Co^{3+} redox potential to lower voltages more capacity can be exploited from the Co^{2+}/Co^{3+} redox pair in $LiCo_{1-y}Fe_yPO_4$ than in pure LCP (upon cycling in the 3.0-5.0 V range).

In addition to their electrochemical properties, olivine materials also exhibit complex magnetic properties.[27-33] Understanding the magnetism of electrode materials can be important when attempting to enhance electrochemical performance.[34-36] LCP has an orthorhombic crystal structure containing four magnetic sub-lattices in the unit cell, which are occupied by high spin (HS) Co^{2+} ($3d^7$, $S = 3/2$) ions. These magnetic centers are ordered collinearly, in an antiferromagnetic (AFM) manner at 23 K.[37] In contrast, a recent neutron-diffraction experiment indicated that in the AFM phase, the magnetic moments are not strictly aligned along the *b*-axis, but rather rotated uniformly from this axis by an angle of ca. 4.6º.[28, 30] This suggests that LCP exhibits a non-collinear type of magnetic structure. Similarly, LFP also forms an orthorhombic crystal structure (space group Pnma),[38] and its unit cell contains four magnetic sub-lattices occupied by HS Fe^{2+} ($3d^6$, $S = 2$) ions. At temperatures below the Néel temperature, i.e. $T<T_N = 50$ K, the Fe^{2+} magnetic moments are ordered in a so-called C-type AFM structure, with collinear ordering.[39, 40, 37, 41] However, recent neutron scattering measurements suggest a different kind of magnetic structure, wherein the magnetic moments lie along the (010) direction, with a slight rotation along this axis. Hence, LFP also exhibits a non-collinear magnetic structure, like LCP. This suggestion received support from first-principles calculations, which attempted to rationalize the observed magnetoelectric (ME) effect (i.e. a phenomenon of inducing magnetic (electric) polarization by applying an external electric (magnetic) field). Specifically, it was suggested that the ME effect in LFP may be attributed to canted spins (i.e. presence of a non-collinear magnetic structure), analogous to

the case of LCP.[42-45] Thus, the spin orientation (i.e. collinear vs non-collinear) in the AFM state in LCP and LFP remains controversial, due to the diverging interpretation of the experimental data on magnetic structure.[37, 41-43] To the best of our knowledge, the magnetic properties of mixed olivine materials have not yet been studied.

In the present study, we adopted a microwave-assisted non-aqueous sol-gel synthetic pathway to form $LiCo_{1-y}Fe_yPO_4$ solid solutions. Subsequently, we fully characterized the structural and magnetic properties of the materials, and addressed controversial issues on their magnetic nature. The measured and computed magnetic moments were compared, and the contribution of the orbital moment was emphasized. Additionally, the ground state spin-orientation of the magnetic ions, i.e. easy vs hard magnetization axis, was calculated for the $LiCo_{1-y}Fe_yPO_4$ solid solutions. Finally, we investigated an exchange mechanism possibly responsible for observed antiferromagnetism in these materials.[30, 39, 46, 47]

(2) Experimental and Computational Methods

2.1 Experimental details

Materials:

Anhydrous iron(II) acetate (STREM chemicals, 97%), anhydrous cobalt(II) acetate (Alfa Aesar, 98+%), anhydrous lithium chloride (Fisher Scientific), phosphoric acid, pure (ACROS Organics) and benzyl alcohol (ACROS Organics, 98+%, extra dry) are stored in a glove box (N_2 filled, O_2< 1 ppm, H_2O< 1 ppm). Diethylene glycol (Alfa Aesar, 99%) is degassed and stored on molecular sieves.

Synthesis of $LiFePO_4$ particles: Iron(II) acetate (1 mmol), lithium chloride (1 mmol), phosphoric acid (1 mmol) and 5 ml of benzyl alcohol are added to a special sealed vial for microwave reaction (CEM Discover) and heated at 180 ˚C (300 W, run time 5 min, hold time 3 min). Ethanol (30 mL, analytical grade) is added, and the dispersion is centrifuged at 3500 rpm for 5 min. After discarding the clear supernatant, the light green precipitate is redispersed in ethanol. This procedure is repeated twice and the light green powder is dried in the oven at 80^{o}C overnight.

Synthesis of $LiCoPO_4$ particles: Cobalt(II) acetate (1 mmol, 177.02 mg), Lithium chloride (1 mmol, 42.39 mg), Phosphoric acid (1 mmol, 98 mg) are added separately to a special sealed vial for microwave reaction (CEM Discover) in diethylene glycol (2 ml, 2 ml and 1 ml respectively). Each precursor is separately dissolved in the solvent before mixing. The homogeneous dark blue solution is placed in a microwave reactor and heated at 270 ^{o}C (300 W, run time 5 min, hold time 60 min). Ethanol (30 mL, analytical grade) is added, and the dispersion is centrifuged at 3500 rpm for 5 min. After discarding the blueish supernatant, the purple precipitate is redispersed in ethanol. This procedure is repeated twice and the purple powder is dried in the oven at 80^{o}C overnight.

Syntheses of $LiCo_{1-x}Fe_xPO_4$ (x = 0.25, 0.50 and 0.75) particles: Solid solutions one step syntheses were developed based on the single phase reactions above; the precursor solution for the solid solutions $LiCo_{1-x}Fe_xPO_4$ is prepared by addition of cobalt(II) acetate and Iron(II) acetate (3:1, 1:1 or 1:3), Lithium chloride and Phosphoric acid (1:1.5:1.5 respectively) are added separately to a special sealed vial for microwave reaction (CEM Discover) in diethylene glycol (2 ml, 2 ml and 1 ml respectively). Each precursor is separately dissolved in the solvent before mixing. The homogeneous dark blue solution is

placed in a microwave reactor and heated at 270 ^{o}C (300 W, run time 5 min, hold time 60 min). Ethanol (30 mL, analytical grade) is added, and the dispersion is centrifuged at 3500 rpm for 5 min. After discarding the blueish supernatant, the purple precipitate is redispersed in ethanol. This procedure is repeated twice and the purple powder is dried in the oven at 80 ^{o}C overnight.

Characterization:

HR-SEM images are collected on a FEI Magellan equipped with an Energy-Dispersive X-ray (Oxford 80 mm^2) spectroscopy (EDS) attachment. EDS is collected on images of 25 μm^2 to facilitate statistical analysis on different regions and a reliable composition. The phase analysis is identified from as-obtained powders by a D8 Advance diffractometer (Bruker) using Cu Kα radiation (λ = 1.54 Å), and operated at 40 mA and 40 kV.

Magnetic properties are measured using a Superconducting Quantum Interference Device (SQUID) magnetometer MPMS XL7. The temperature-dependent susceptibility is measured in a temperature range of 200 to 4 K at a constant field of $\mu_0 H$ = 0.05 T.

2.2 Computational details

The employed unit cells exhibit a layered structure, where each magnetic layer is separated by nonmagnetic Lithium (Li), Phosphorus (P) and Oxygen (O) layers as shown in Fig. 1A. Each P ion is tetrahedrally coordinated to O, whereas Fe, Co, and Li ions occupy the centers of distorted oxygen octahedra. All the DFT calculations were performed using the VASP code and projector augmented wave (PAW) pseudopotentials within the generalized

gradient approximated (GGA) formalism in conjunction with Hubbard corrections (GGA+U).[48-50] For the exchange-correlation potential, we use the GGA Perdew-Burke-Ernzerhof (PBE) functional[51] modified for solid-state systems with U correction (PBEsol-GGA+U), previously suggested by Osnis *et al.*[24] We used U values of 5.3 and 6.7 eV for the Fe and Co atoms, respectively, while X = 1.0 eV in all the cases, based on the work of Osnis et al. and Zhou et al.[24, 52 42] In addition, the value of X was also tuned to obtain the correct canting angle for the pure olivines. All the aforementioned structures and cell parameters were fully relaxed with antiferromagnetic ordering for each type of calculation. The convergence of the total energy was verified with respect to the energy cutoff, which was ultimately set to 500 eV. The Monkhorst-Pack scheme for k-point sampling was used for integration in the irreducible Brillouin zone (BZ).[53]

All the calculations including SOC, were performed in the non-collinear mode implemented in VASP by Hobbes et al.[54] and Marsman and Hafner.[55] Here, we map self-consistent DFT total energies of several non-collinear magnetic configurations, obtained by constraining the magnetic moment along a specific direction, onto a general spin-depend Hamiltonian. Moreover, within the Kohn-Sham DFT framework, noncollinearity is handled by generating the orbitals as complex spinors, resulting in a 2×2 density matrix, $\rho^{\alpha\beta}(r)$ (Eq. 1). [43]

$$\rho^{\alpha\beta}(r) = \sum_i f_i \, \psi_i^{\alpha*}(r)\psi_i^{\beta}(r) \qquad (1)$$

where f_i is the orbital occupancy number and $\psi_i^{\alpha/\beta}(r)$ is the ground state wave function. The equivalent magnetization density m(r) can be computed using the following transformation[54]:

$$\overrightarrow{m(r)} = \sum_{\alpha\beta} \rho^{\alpha\beta}(r).\ \sigma^{\alpha\beta} \qquad (2)$$

where $\vec{\sigma} = (\sigma_x,\ \sigma_y,\ \sigma_z)$ are the Pauli spin matrices, which are defined as

$$\sigma_x = \begin{pmatrix} 0 & 1 \\ 1 & 0 \end{pmatrix},\ \sigma_y = \begin{pmatrix} 0 & -i \\ i & 0 \end{pmatrix},\ \sigma_z = \begin{pmatrix} 1 & 0 \\ 0 & -1 \end{pmatrix},$$

Hence, the magnetization density is invariant in both magnitude and direction throughout the system. For the noncollinear calculation the exact Kohn-Sham Hamiltonian becomes a 2×2 matrix as shown below[56]

$$H_{KS}^{\alpha\beta}(\mathrm{r}) = -\hbar^2\nabla^2/2\mathrm{m_e} + V_{KS}^{\alpha\beta}(r) \qquad (3)$$

Thus, by solving the above set of expressions a possible ground state orientation of the magnetization density at point *r* can be obtained. Hence, the canting angle, which is a geometrical angle between the magnetization density and a given quantisation axis, can be estimated for a system.

For all the composition, the total density of states obtained by different methods is shown in Fig. 6(a). Additionally, to understand the path of the exchange interaction, we computed Wannier functions of the low-lying occupied bands of the minority spin of the Fe-$3d_{z^2\text{-}r^2}$ orbital using the wannier90 code (without inclusion of spin-orbit effects).[57]

(3) Results

3.1 Synthesis and structural properties

$LiCo_{1-x}Fe_xPO_4$ (x = 0.00, 0.25, 0.50, 0.75, 1.00) were synthesized using a microwave-directed non-aqueous liquid phase synthesis approach, as suggested by Bilecka et al. for LFP. [58] In comparison to traditional solid-state routes, the current reaction temperatures are much lower and the reaction times are significantly shorter. All the samples were carefully characterized by X-ray diffraction (XRD) combined with Rietveld analysis, Scanning Electron Microscopy (SEM) with energy-dispersive X-ray spectroscopy (EDS) and elemental analysis (ICP-AES). Morphological details for $LiFePO_4$ and $LiCoPO_4$ were obtained by SEM, revealing a platelet-like shape in the micrometer size-range (Fig. S1). The solid solutions display a flower-like assembly of platelets on the micrometer scale (Fig. 2). The elemental analysis of the samples follows the stoichiometry of the reagents and ICP-AES measurements are in agreement with the input ratio (Table S1). The studied orthophosphates $LiCo_{1-x}Fe_xPO_4$ (x = 0.00, 0.25, 0.50, 0.75, 1.00) crystallize in the orthorhombic olivine structure with space group Pnma, which can be inspected from our measured XRD patterns (Fig. 3). The measured experimental XRD patterns are consistent with earlier reported patterns[12] for both pure and mixed systems. The lattice constants of the different phosphates are summarized (Table S2) and agree well with the literature and our computed data. Comparison of the experimental and calculated XRD patterns (Rietveld refinement) reveals a very good agreement, confirming the presence of $LiFePO_4$ and $LiCoPO_4$ phases as the only crystalline phase in the powder (Fig. S2). A systematic shift for the diffraction peaks of the XRD patterns clearly shows the formation of single-phase solid solutions (Fig. 3).

In order to simulate the substitution of Fe at the Co site, we constructed supercells with size dependence on the concentration (x) of the excess Fe at the Co site. For LCP and LFP, we have used four formula unit cells, while for the mixed systems, we employed eight

formula unit supercells to simulate a fully relaxed AFM configuration. All the model structures are shown in Fig. S3.

3.2 Experimental Magnetic properties

The temperature dependence of the magnetic susceptibility was measured at low field $\mu_0 H$ = 0.05 T. The samples are paramagnetic at room temperature and exhibit a phase transition to antiferromagnetism at a critical temperature. The critical temperature (or Néel Temperature) corresponds to the maximum of magnetic susceptibility χ (Fig. 4a) or to the deviation from the Curie law of the inverse of the susceptibility $1/\chi$ (Fig. 4b). The variations of the Néel temperature and the experimental effective moment may be deduced from Curie-Weiss law linear fitting above the Néel temperature (Fig. 4b-c). The Curie constant and the Weiss temperature have been calculated for all samples and are reported in the figures for the solid solutions. As expected, the negative Weiss temperature reflects antiferromagnetic interactions between the spins. The Néel temperature increases almost monotonically from T_N = 22 K for LCP to T_N = 52 K for LFP (Fig. 4d), consistent with the literature (refer Table I). This gradual increase is a good indication of the homogeneity of the solid solution.

More surprisingly, the effective magnetic moment of LCP is found to be very high with a value of 4.77 μ_B/formula unit, compared to the spin-only value for HS Co(II) compounds, which is 3.87 μ_B/Co (Table I). Similarly, LFP exhibits 5.44 μ_B/formula unit compared to the spin-only value of 4.89 μ_B/Fe. The magnitude of the effective magnetic moment (μ_{eff}) has been debated in the literature for pure olivines.[30, 32, 37-39, 59-61] It has been found experimentally that the observed magnitude of μ_{eff} can exceed the spin-values of 3.87 μ_B and 4.89 μ_B for both the pure olivines, LCP and LFP, respectively. Indeed, these spin-only

values are expected only for octahedrally coordinated, HS Co-3d^7 and Fe-3d^6 configurations with full quenching of the orbital moments.

Interestingly, an increasing trend of the effective magnetic moment was not observed upon incorporation of HS Fe^{2+} ion in place of HS Co^{2+} ion (Fig. 4d), which in principle gives an extra spin magnetic moment (Table I). We also note that the effective magnetic moments are not additive, and hence for the mixed olivines, where different magnetic centers are present in the material, the average effective magnetic moment was estimated as discussed by Chernova *et al.* [35] The above μ_{eff} trend could be a result of unquenched orbital moments, suggesting that first-principles calculations might be able to explain the various contributions to the observed μ_{eff} for LCP, LFP and the solid solutions.

3.3 Computed Magnetic Structure and Magnetic Properties

(A) Magnetic structure: Possible orientations of spin and orbital magnetic moments

We computed both the spin and orbital magnetic moment orientations for the magnetic ions in all the olivine compositions (Fig. 5). Initially, a careful analysis of the relative energy of the unit cells for different plausible magnetic structures, as well as for different spin quantization directions was compared (Fig. 1 b and c, respectively). All subsequent calculations and analyses were performed on the ground state magnetic structure of the $LiCo_{1-x}Fe_xPO_4$ systems. Results presented in Fig. 5 (b, f), clearly confirm that the pure analogues, LCP and LFP, form a non-collinear magnetic structure with an observed canting angle in agreement with neutron diffraction studies on the single crystals of LCP and LFP.[30, 62] We note that the magnitude of the canting angle also depends on the value of the exchange

(X) parameter, as discussed by Bousquet et al.[63] We also observe the same X-dependent behavior, as shown in the SI (Fig. S4). An optimal magnitude of the canting angle of 4.58° is obtained with X = 0.4 eV (Fig. 5b), and is in good agreement with the experimental canting angle of 4.6º.[30] However, using this X-value, the easy axis is oriented incorrectly along the a-direction. This can possibly be due to a large canting of the spins for a given axial spin quantization direction, which will lead to a plane anisotropy in LCP, which therefore cannot be disregarded for this material.

To clarify the issue of the incorrect orientation of spins in LCP, we also compared the energy of the unit cell by quantizing the spin along the [011] and [111] plane directions. We found that the energy of the unit cell is indeed lower in the [011]-quantized direction compare to other directions, as shown in Fig. S5. We also compared the electronic structure of LCP with spin quantization along the plane directions [011] and [101], and conclude that these are invariable (Figure S6). Thus, the preferred spin-orientation for LCP is in the [011] or bc plane (i.e. easy plane anisotropy), while for LFP the preferred spin-orientation is approximately along the b-axis (i.e. easy axis anisotropy) with a slight rotation from this axis. Thus, LFP is more prone to display axial anisotropy with a small canting angle of ca. 1º (Fig. 5f). This is consistent with previous studies.[39, 62]

Our calculations also reveal that for all the solid solutions, the Co and Fe spins have a small canting angle with the easy axis, after optimizing both the spin and atomic structure starting from an AFM configuration (Fig. 5c-e). Thus, all the studied compositions apparently show a non-collinear type magnetic structure. To the best of our knowledge, no experimental literature data are available to compare the magnetic structure of mixed olivines. Besides the

complex magnetic structure, the studied olivine compounds also exhibit complex magnetic properties that will be discussed in the following section.

(B) Magnetic properties of pure and mixed olivines

In general, when there is no orbital angular momentum associated with the metal ion centers, the effective magnetic moment may be expressed as $\mu_{eff} = g * \sqrt{S(S+1)}\mu_B$. Here *g* is the spectroscopic splitting factor, or the magnetomechanical factor, which depends on the experimental tools,[64] and is equal to two in the spin-only case, but may deviate from this value due to spin-orbit interactions. However, in reality, transition metals often have a non-negligible orbital angular moment.

In an ideal Fe/CoO_6 octahedra, the fivefold degenerate energy of the Fe-3*d* states splits into two subsets: a lower, threefold set of t_{2g} levels and a higher, twofold set of e_g levels. Interestingly, in all the studied compositions, the crystal field splitting is lower than the Hund spin-exchange (spin-flip) energy for Co^{2+} and Fe^{2+} ions (Fig. 6b). Consequently, the HS state is obtained for these ions. According to Hund's rule, in the ground state of the HS Fe^{2+} ($3d^6$) and Co^{2+} ($3d^7$) ions, each of these five 3*d* orbitals are filled with spin-up electrons, while the spin-down t_{2g} orbitals are filled with one and two electrons, respectively. This can be observed in the orbital projected density of states for the Co^{2+} and Fe^{2+} ions (Fig. 6b).

Because of this low-crystal field *d*-band splitting, which results in a high-spin state, the orbital angular momentum, *L*, is *not* quenched (i.e. $\langle\psi|L|\psi\rangle \neq 0$). In such a case, the resulting electronic states are described by the orbital and spin quantum numbers, *L* and *S*. We hypothesize that in LFP and LCP, the existence of partially filled t_{2g} orbitals in the down spin channel of both Co^{2+} and Fe^{2+} ions results in an unquenched orbital moment.

In view of the above, we computed the average orbital and spin magnetic moment on the Co^{2+} and Fe^{2+} ions, for each composition in $LiCo_{1-x}Fe_xPO_4$ (Fig. 7 a, b). An increase in the average spin magnetic moment as a function of x was observed in $LiCo_{1-x}Fe_xPO_4$ (Fig. 7a). This is expected as we are incorporating Fe^{2+} ions, having four unpaired electrons, at the expense of Co^{2+} ions, which have only three unpaired electrons. The computed value of the spin magnetic moment for pure LFP (3.72 μ_B) is in good agreement with the experimentally determined value 3.93 μ_B by inelastic neutron scattering measurements (refer Fig. 7a).[62] On the other hand, the computed average orbital moment continuously decreases as a function of x (Fig 7b). Surprisingly, the average orbital moment (per magnetic ion) was reduced by almost 50% (from 0.522 μ_B to 0.23 μ_B) as Fe^{2+} is introduced into LCP (i.e. the case for x = 0.25) (Fig. 7b). In particular, this effect is pronounced for the Co^{+2} ions (inset in Fig. 7b). For $x \geq 0.25$ systems, there were only minor changes in the orbital moment for Co^{2+} and Fe^{2+}. We also note that in general, the Co^{2+}-orbital moment is greater than for Fe^{2+} in both the pure materials and the solid solutions (inset of Fig. 7b).

Next, we shall compute the value of $\mu_{eff,}$ with the help of the values of L and S obtained using DFT calculations. The effective magnetic moments for such materials can be predicted using the following equation, as suggested by Chernova et al:[35]

$$\mu_{eff} = \sqrt{L(L+1) + 4 * S(S+1)}\,\mu_B \qquad (4)$$

Here, L and S are not added up to form the total angular momentum, J, and hence give rise to an uncoupled atomic magnetic moment, as can be observed in the case of paramagnetic materials. On the other hand, one may assume that L and S are strongly coupled and add up to form, J. In this latter case, according to Hund's rule, the level with the highest value of J has

the lowest energy due to a more than half-filled outmost subshell of Fe^{2+} and Co^{2+} ions. This rule can only be applied in the *LS* coupling regime (i.e. Russell-Saunder coupling, where **J** = $\sum l_i + \sum s_i = \mathbf{L} + \mathbf{S}$, where l_i and s_i are the orbital and spin moment of the electrons, respectively (Fig. 5a). In this case, the equation for μ_{eff} takes the following form:[65]

$$\mu_{eff} = g_{exp} * \sqrt{J(J+1)}\mu_B \qquad (5)$$

In computing the effective magnetic moment (Eq. 4 or 5), we employ DFT to extract the spin magnetic moment (μ_s) and orbital magnetic moment (μ_l) to obtain *L*, *S*, and *J*. The Landé *g*-factor was obtained from experiment, although we also attempted to use the theoretical value (i.e. $g = 2$) (Table I). In Table I we report the computed, experimental and literature values for μ_{eff}.

A survey of the literature reveals that there is significant disagreement between the different reported values of *g* and μ_{eff} for the pure olivines, LCP and LFP. For instance, the value of *g* for a single crystal (SC) of LCP is 2.17,[30] while for the polycrystalline (PC) sample, the reported value by Baek et al. is 2.27.[60] Our experimental value is 2.36 for a PC sample (Table I). Similarly, for LFP, the value of *g* for the SC sample varies from 2.02- 2.22, depending on the spin quantization axis.[32] Our experimental *g*-value for LFP is 2.002 for a PC sample (Table I). Consequently, the value of μ_{eff} ranges from 4.2 to 5.7 μ_B in LCP, [30, 37, 38, 60, 61] while it varies from 4.95–6.8 μ_B[32, 38, 39, 62] in LFP, depending on the given experimental conditions (i.e. *g*-value). Nevertheless, both the computed and experimental effective magnetic moments for LCP and LFP are larger than the theoretically estimated spin-only value of 3.87 μ_B and 4.89 μ_B, respectively (i.e. the orbital angular momentum is fully quenched by the crystal field). Hence, an unquenched orbital moment results in increased

effective magnetic moments, as is observed for LFP and LCP. This behavior is observed in all the mixed composites as well (Table I).

In-stead of using Eq. 4 or 5, one may employ the following expression for the effective magnetic moment:

$$\mu_{eff} = \sqrt{L(L+1)} + g_{exp} * \sqrt{S(S+1)}\,\mu_B \qquad (6)$$

Here, the first term is the magnitude of the orbital moment (μ_l) and the second term is the magnitude of the spin moment (μ_s), and the experimental *g*-value is used. Using Eq. 6 we obtain effective magnetic moments of 5.22 μ_B, 4.63μ_B, 4.80 μ_B, 4.67 μ_B, and 5.01 μ_B for the compositions x = 0.00, 0.25, 0.50, 0.75, and 1.00. This formulation yields overall better agreement with the experimental value of μ_{eff} than with Eq. 4 and 5, with the exception of x = 0.00. However, for the pure LCP system we obtain better agreement with the experimental value of 4.77 μ_B using Eq. 5, where we get μ_{eff} = 4.58 μ_B. This indicates that there is strong SOC in LCP. This is due to a significant SOC, a point that will be discussed further below. Therefore, the inclusion of SOC in the calculations, is essential to obtain qualitative agreement with the observed effective magnetic moments.

3.4 Origin of the large orbital angular momentum of Co^{2+}/Fe^{2+}in the HS state

The SOC and its partial quenching in several transition-metal based compounds have been studied by Goodenough and Ham et al.[66, 67] In an ideal octahedral arrangement (i.e. a cubic symmetric crystal field), Co^{2+} and Fe^{2+} ions do not exhibit orbital magnetic moments. However, according to Okamoto et al., breaking of a cubic (O_h) symmetry to a tetragonal

(D_{4h}) symmetry leads to a considerable orbital moment on the magnetic ions. Even so, this is only possible if the tetragonal crystal field splitting is smaller than the SOC ($\Delta t_{2g} << \lambda$), and hence the t_{2g} orbitals mix and give rise a large orbital angular momentum.[68, 69] A schematic representation of the electronic structure for the t_{2g} and e_g orbitals in the presence of cubic and tetragonal environments, and an accompanying detailed discussion, are presented in the Supplementary Information (p. S11).

In order to estimate the importance of the orbital moment and SOC, it is useful to compare the strength of the SOC energy with the tetragonal splitting energy. The required values for the expectation value of the SOC energy, E_{soc}, for Co^{2+} and Fe^{2+} ions, can be obtained by the following equation (Fig. 8a, b):

$$<E_{soc}> = < \frac{1}{c^2}\frac{1}{r}\frac{dV}{dr}\hat{l}\cdot\hat{s} > \qquad (7)$$

where c is the velocity of light, r is the radial distance in each atomic sphere, V is the effective potentials function of r, and $\hat{l}$ and $\hat{s}$ are the orbital and spin operators, respectively.[70, 71] The strength of the tetragonal crystal field splitting can be estimated by calculating the average energy value, $<E>$, for each l and m_l-decomposed 3d states below the Fermi level (i.e. valence band) for both Co^{2+} and Fe^{2+} ions, using the following equation:

$$< E > = \frac{\int_{-\infty}^{E_F} E\ DOS(E, lm)\ dE}{\int_{-\infty}^{E_F} DOS(E, lm)\ dE} \qquad (8)$$

This expression provides the average energy for each orbital below the Fermi level. The computed average energies are shown in Fig. 8c and d for Co^{2+} and Fe^{2+}. Firstly, we discuss the Co^{2+} ion in the x = 0.00 and 0.75 compositions, where the average energy value for each t_{2g} orbital clearly indicates a tetragonal type splitting in the t_{2g} manifold. The

corresponding average t_{2g}-values are as follows: $< E >_{0.00}^{|xz>}$= 4.00 eV, $< E >_{0.00}^{|yz>}$ = 4.13 eV, and $< E >_{0.00}^{|xy>}$ = 3.70 eV; $< E >_{0.75}^{|xz>}$ = 5.60 eV, $< E >_{0.75}^{|yz>}$ = 5.43 eV, and $< E >_{0.75}^{|xy>}$ = 4.00 eV. This suggests that the tetragonal splitting Δt_{2g} ($i.e.(< E >^{|yz>} + < E >^{|xz>})/2 - < E >^{|xy>}$) is 0.55 eV and 1.55 eV for the systems with x = 0.00 and 0.75, respectively. This is significantly larger than the SOC energy of 61.4 meV and 23.2 meV for the x = 0.00 and 0.75 compositions, respectively (refer Fig. 8a). Therefore, the entire orbital moment should be quenched for these compositions. Therefore, the aforementioned hypothesis that t_{2g} orbital-mixing may give rise to unquenched orbital moment does not hold for these compositions. Thus, the calculated large orbital moments on Co^{2+} ions for x = 0.00 and 0.75 composition can only be explained on the basis of the population imbalance of the e_g orbital, as is the case for $KOsO_4$ as discussed by Song et al.[72]

The above argument can be solidified through the calculation of the occupation of the m_l = +2 (x^2-y^2) and m_l = -2 (xy) orbitals. Using the PBE+U electron density, we analyzed the occupancy of the each orbital corresponding to different azimuthal quantum number (m_l), by integrating out the lm_l-decomposed density of states for each spin channel up to the Fermi level (Fig. 9).[73] The occupancies of the 3*d*-orbitals in the up-spin channel for both Co^{2+} and Fe^{2+} ions (Fig. 9 a, c) remain almost constant for all compositions, indicating completely filled orbitals with full occupancy of almost one. In contrast, we do observe variations in the occupancies for all the orbitals of Co^{2+} in the down spin channel (Figure 9b). This is particularly so for the xy and x^2-y^2 orbitals, where the occupancy changes from minimum values of 0.05 and 0.07 to maximum values of 0.88 and 0.83, respectively. In particular, we observe an occupation difference between the xy and x^2-y^2 orbitals of 0.43 for x = 0.00 and 0.81 for the x = 0.75 system. Thus, the above hypothesis of the occupancy difference in the

e_g-regime (i.e. xy and x^2-y^2) is a plausible reason for the proposed unquenched orbital moment in Co^{2+} for the x = 0.00 and 0.75 compositions.

For the remaining compositions (i.e. x = 0.25 and 0.50), the Co^{2+}-ion tetragonal crystal field splitting is not as strong as for the x = 0.00 and 0.75 compositions (Fig. 8c). The most probable energies for the |xy>, |yz> and |xz> orbitals for the x = 0.25/0.50 compositions are 6.01/4.99 eV, 5.90/4.80 eV, and 5.83/5.20 eV, respectively. Therefore, mixing of the t_{2g} orbital may lead to some finite orbital moment in these compositions.

On the other hand, for the Fe^{2+} ions, at all compositions, we do not observe any noticeable tetragonal crystal field splitting (Fig. 8d). Surprisingly, we find that all the t_{2g} orbitals are almost non-degenerate, having most probable energy values for |xy>/|yz>/|xz> orbital of 4.36/4.35/3.27, 4.41/4.24/3.24, 3.18/4.18/2.79, and 4.32/4.10/3.29 eV for x = 0.25, 0.50, 0.75, and 1.00, respectively. Thus, mixing of t_{2g} orbitals does not occur in these cases. Furthermore, we also note that there is a substantial imbalance in the occupation of the m_l = +2 (x^2-y^2), and m_l = -2 (xy) orbitals in the spin-down channel (Fig. 9d) for the Fe^{2+} ions. The occupation changes from a minimum value of 0.04 and 0.16 to a maximum value of 0.05 and 0.50 for xy and x^2-y^2 orbitals, respectively. Therefore, the unquenched orbital moment can be attributed to occupancy differences between the xy and x^2-y^2 orbitals for the Fe^{2+} ions for all the compositions.

3.5 Possible mechanism behind the antiferromagnetic exchange interaction

Experimentally, the observed increase in the Néel temperature (T_N) of $LiCo_{1-x}Fe_xPO_4$ with x (refer Fig. 4d or Table I) is directly related to the strength of the dipolar exchange interactions between the magnetic ions. Previously, several exchange mechanisms have been proposed for transition metal based AFM oxides. For instance, the well-known Goodenough-Kanamori-Anderson (GKA) super exchange interaction (SEI) mechanism via oxygen (O) (M – O – M; M = transition metal), includes only in-plane interaction.[74, 75] Also, the super-super exchange interaction (SSEI) mediated by two oxygen atoms (M – O – O – M) (also includes out of plane interaction through O)[76] are proposed for general metal oxide system, and SSEI via phosphorous and oxygen atoms (M – O – P – O – M)[77] (includes out of plane interaction through both O and phosphorous ions) is suggested for phosphate polyanion-based oxides.

In the view of the above, we analyze the following: Metal (M) – Oxygen (O) bond length, M – O – M bond angle, and the magnetic moment on oxygen ions i.e. polarization of oxygen ions (refer Figures S11 and S12), which might be responsible for the transfer of out of plane interactions. Surprisingly, we did not observe any such trend in the bond angle and oxygen ions polarization as a function of x, which can explain the rising trends in the Néel temperature. Hence, in the current study, SEI and SSEI paths cannot explain the observed rising trend in the Néel temperature, although another remaining possibility is SSEI. Indeed, using a Wannier function analysis, we find that the rising trend in Néel temperature can be understood with the help of SSEI via phosphorous and oxygen atoms (M – O – P – O – M).[77]

This analysis is based on the assumption that if the low-energy sets of bands are separated from all other bands, chemically accurate Hamiltonians are constructed directly in the Wannier basis. This method has been successfully employed to analyze the electronic structure and facilitate direct visualization of the various interaction paths of a number of

materials.[77-79] In the current case, introduction of Fe^{2+} changes the electronic structure in pure LCP and as a result, iron $3d_{z^2-r^2}$ states appear near the Fermi level (Fig. S7), and these states are well separated from all other bands. We note that the above method cannot be applied to LCP, because there is no distinct separation of the band being analyzed and all other bands, due to strong orbital hybridization among Co-*d*, as well as O-2*p* states (Fig. S9) Inspection of the Wannier functions shows that the Fe^{2+} $3d_{z^2-r^2}$ orbital is primarily localized on the FeO_6 octahedra, with minor out-of-plane hybridization with oxygen, mediated via P (see arrow in Figure 10a). Therefore, a possible out-of-plane M – O – P – O – M exchange path exists for both mixed and LFP systems. We cannot rule out that this exchange path also exists in LCP.

4. Discussion

The results of our DFT calculations in the preceding section clearly suggest that inclusion of SOC is important in theoretical treatments of olivines. Additionally, with the help of Wannier function analyses, we were able to propose that the M – O – P – O – M interaction is a possible exchange path, underpinning the magnetic properties of $LiCo_{1-x}Fe_xPO_4$ compounds.

We find that Co^{2+} exhibits a strong orbital moment in the pure LCP system, which is partially quenched by the substitution of Co by Fe. We also observe a significant orbital moment on the Fe-ions, which cannot be neglected. Our calculations suggest that a non-collinear magnetic structure is present in $LiCo_{1-x}Fe_xPO_4$ for all the compositions.

Interestingly, our calculations clearly revealed that the observed orbital moment in the studied olivines is not only due to weak tetragonal splitting seen in the t_{2g} orbitals manifold, but also due to a population imbalance in the e_g orbital manifolds of the Co^{2+} and Fe^{2+} ions. For the compositions x = 0.00 and 0.75, the origin of the orbital moment on Co^{2+} ions can be explained with the help of imbalance in the occupations of the xy and x^2-y^2 orbitals in the spin-down channel. On the other hand, for x = 0.25 and 0.50, it appears that the orbital moment is due to weak tetragonal crystal field splitting. For the Fe^{2+} ions, the root of the orbital moment cannot be explained by tetragonal crystal field splitting because of the non-degenerate t_{2g} orbitals. On the other hand, our calculation has revealed that there is substantial population imbalance in e_g orbitals, which leads to unquenched orbital magnetic moments on the Fe ions.

Using Wannier functions, we have also shown that the SSEI M – O – P – O – M interaction is a potentially important mechanism underlying the magnetism in the mixed olivines. We find that the symmetry of the tail of the Fe $3d_{z^2-r^2}$ orbital allows it to form pd π antibond with the O-p_x/p_y orbitals. To achieve orbital overlap, the tail of the O-p_x/p_y orbitals bends towards the Fe atom. Moreover, we find that the bending of the O-p_x/p_y tail is not only towards P (i.e. suggesting M - $[PO_4]_{tetra}$- M interaction), but also towards the nearest neighboring Co ions for the x = 0.25 composition (refer Figure S13). Surprisingly, for x = 1.00, we did not observe any such bending of the O-p_x/ p_y tail towards the nearest neighbor Fe (refer Figure S14).

Therefore, the magnetic interaction of the pure LFP system is affected by the presence of Co and changes both in plane AFM Fe – O – Fe, as well as out of plane FM Fe – O – P – O – Fe exchange interactions. It can also be observed experimentally that in the LCP system,

the nearest neighbor, out of plane exchange interaction ($J_\perp$), is 8 times stronger than in pure LFP.[33, 62] The existence of a C-type AFM magnetic structure for LFP implies that the out of plane interaction must be FM. [63] Therefore, increasing the amount of Co atom will likely strengthen the out of plane FM interactions in $LiCo_{1-x}Fe_xPO_4$, and as a consequence, the strength of the net AFM exchange weakens. This will lead to a decrease in the Néel temperature (T_N) with the amount of Co.

(5) Conclusions

We presented a novel synthesis of $LiCo_{1-x}Fe_xPO_4$ (x = 0.00, 0.25, 0.50, 0.75, 1.00), which was obtained by microwave assisted non-aqueous sol-gel synthesis. The synthesis yields platelet-like micron-scale particles with an olivine crystalline structure. The magnetic susceptibility measurements reveal high experimental effective magnetic moment compared to the spin-only values, which is in agreement with previous results. Inclusion of SOC in first-principles DFT calculations results in good agreement between computed and experimental effective magnetic moments. Furthermore, our calculations revealed that a non-collinear magnetic structure is present in $LiCo_{1-x}Fe_xPO_4$ for all the compositions. Our calculation also revealed that the canting angle strongly depends on the value of the exchange parameter, X, in the strong SOC limit (e.g. LCP).

Additionally, our results show that the metal ions have a non-negligible orbital angular moment. For the Co^{2+} ions, the source of the orbital moment can be explained by considering the imbalance in the m_l = +2 (x^2-y^2) and m_l = -2 (xy) orbital occupations for the down – spin channel for the compositions x = 0.00 and 0.75. For the x = 0.25 and 0.50 compositions, a weak tetragonal crystal field splitting (Δt_{2g}) has to be taken into account to

understand the large orbital moment on Co^{2+} ions. In the case of the Fe^{2+} ions, the presence of an orbital moment can only be explained by population imbalance in the e_g orbitals of the Fe^{2+} ions for all the presented compositions.

Finally, Wannier functions were used to understand the observed rising trend in the Néel temperature, which is directly related the exchange interaction paths in the materials. We have found for the first time that out of layer M – O – P – O – M magnetic interactions ($J_\perp$) are present in the studied materials, something which thus far remained a speculation only.[39, 47] Using the spread of the Wannier function of the Fe-3$d_{z^2-r^2}$ orbital, we concluded that the presence of more Co will lead to stronger FM out of plane M – O – P – O – M interaction and as a consequence the strength of the total AFM exchange becomes weaker and hence the Néel temperature (T_N) decreases.

References

1. V. Etacheri, R. Marom, R. Elazari, G. Salitra and D. Aurbach, *Energy Environ. Sci.*, 2011, **4**, 3243-3262.
2. B. Scrosati and J. Garche, *J. Power Sources*, 2010, **195**, 2419-2430.
3. G. Nazri and G. Pistoia, *Lithium batteries : science and technology*, Kluwer Academic Publishers, Boston, 2004.
4. M. D. Johannes, K. Hoang, J. L. Allen and K. Gaskell, *Phys. Rev. B*, 2012, **85**, 115106.
5. K. Ozawa, *Solid State Ionics*, 1994, **69**, 212-221.
6. E. M. Erickson, C. Ghanty and D. Aurbach, *J. Phys. Chem. Lett.*, 2014, DOI: 10.1021/jz501387m, 3313-3324.
7. G. Ceder, G. Hautier, A. Jain and S. P. Ong, *MRS Bull.*, 2011, **36**, 185-191.
8. Y. Zhang, Q. Y. Huo, P. P. Du, L. Z. Wang, A. Q. Zhang, Y. H. Song, Y. Lv and G. Y. Li, *Synth. Met.*, 2012, **162**, 1315-1326.
9. W.-J. Zhang, *J. Power Sources*, 2011, **196**, 2962-2970.

10. M. Kaus, I. Issac, R. Heinzmann, S. Doyle, S. Mangold, H. Hahn, V. S. K. Chakravadhanula, C. Kübel, H. Ehrenberg and S. Indris, *J. Phys. Chem. C*, 2014, **118**, 17279-17290.
11. M. Hu, X. Pang and Z. Zhou, *J. Power Sources*, 2013, **237**, 229-242.
12. N. V. Kosova, O. A. Podgornova, E. T. Devyatkina, V. R. Podugolnikov and S. A. Petrov, *J. Mater. Chem. A*, 2014, DOI: 10.1039/C4TA04221B.
13. T. Muraliganth and A. Manthiram, *J. Phys. Chem. C*, 2010, **114**, 15530-15540.
14. S. K. Martha, J. Grinblat, O. Haik, E. Zinigrad, T. Drezen, J. H. Miners, I. Exnar, A. Kay, B. Markovsky and D. Aurbach, *Angew. Chem. Int. Ed.*, 2009, **48**, 8559-8563.
15. B. Zhang, X. Wang, H. Li and X. Huang, *J. Power Sources*, 2011, **196**, 6992-6996.
16. A. Yamada, Y. Takei, H. Koizumi, N. Sonoyama, R. Kanno, K. Itoh, M. Yonemura and T. Kamiyama, *Chem. Mater.*, 2006, **18**, 804-813.
17. G. Li, Y. Kudo, K.-Y. Liu, H. Azuma and M. Tohda, *J. Electrochem. Soc.*, 2002, **149**, A1414-A1418.
18. G. Kobayashi, A. Yamada, S.-i. Nishimura, R. Kanno, Y. Kobayashi, S. Seki, Y. Ohno and H. Miyashiro, *J. Power Sources*, 2009, **189**, 397-401.
19. C. M. Burba and R. Frech, *J. Power Sources*, 2007, **172**, 870-876.
20. I. C. Jang, C. G. Son, S. M. G. Yang, J. W. Lee, A. R. Cho, V. Aravindan, G. J. Park, K. S. Kang, W. S. Kim, W. I. Cho and Y. S. Lee, *J. Mater. Chem.*, 2011, **21**, 6510-6514.
21. S. Yang, V. Aravindan, W. Cho, D. Chang, H. Kim and Y. Lee, *J. Electrochem. Soc.*, 2012, **159**, A1013-A1018.
22. M. V. V. M. S. Kishore and U. V. Varadaraju, *Mater. Res. Bull.*, 2005, **40**, 1705-1712.
23. Z.-P. Lin, Y.-M. Zhao and Y.-J. Zhao, *Chin. Phys. B*, 2011, **20**, 018201.
24. A. Osnis, M. Kosa, D. Aurbach and D. T. Major, *J. Phys. Chem. C*, 2013, **117**, 17919-17926.
25. M. Dixit, H. Engel, R. Eitan, D. Aurbach, M. D. Levi, M. Kosa and D. T. Major, *J. Phys. Chem. C*, 2015, **119**, 15801-15809.
26. F. C. Strobridge, D. S. Middlemiss, A. J. Pell, M. Leskes, R. J. Clement, F. Pourpoint, Z. G. Lu, J. V. Hanna, G. Pintacuda, L. Emsley, A. Samoson and C. P. Grey, *J. Mater. Chem. A*, 2014, **2**, 11948-11957.
27. R. P. Santoro and R. E. Newnham, *Acta Crystallogr.*, 1967, **22**, 344-&.
28. D. Vaknin, J. Zarestky, J.-P. Rivera and H. Schmid, in *Magnetoelectric Interaction Phenomena in Crystals*, eds. M. Fiebig, V. Eremenko and I. Chupis, Springer Netherlands, 2004, vol. 164, ch. 16, pp. 203-217.
29. G. Rousse, J. Rodriguez-Carvajal, S. Patoux and C. Masquelier, *Chem. Mater.*, 2003, **15**, 4082-4090.
30. D. Vaknin, J. Zarestky, L. Miller, J.-P. Rivera and H. Schmid, *Phys. Rev. B*, 2002, **65**, 224414.
31. J. Y. Li, V. O. Garlea, J. L. Zarestky and D. Vaknin, *Phys. Rev. B*, 2006, **73**.
32. G. Liang, K. Park, J. Li, R. E. Benson, D. Vaknin, J. T. Markert and M. C. Croft, *Phys. Rev. B*, 2008, **77**, 064414.
33. W. Tian, J. Li, J. W. Lynn, J. L. Zarestky and D. Vaknin, *Phys. Rev. B*, 2008, **78**, 184429.
34. S. Boyanov, M. Womes, L. Monconduit and D. Zitoun, *Chem. Mater.*, 2009, **21**, 3684-3692.

35. N. A. Chernova, G. M. Nolis, F. O. Omenya, H. Zhou, Z. Li and M. S. Whittingham, *J. Mater. Chem.*, 2011, **21**, 9865-9875.
36. G. Gershinsky, E. Bar, L. Monconduit and D. Zitoun, *Energy Environ. Sci.*, 2014, **7**, 2012-2016.
37. R. Santoro, *J. Phys. Chem. Solids*, 1966, **27**, 1192.
38. M. C. Tucker, M. M. Doeff, T. J. Richardson, R. Fiñones, E. J. Cairns and J. A. Reimer, *J. Am. Chem. Soc.*, 2002, **124**, 3832-3833.
39. R. P. Santoro and R. E. Newnham, *Acta Crystallogr.*, 1967, **22**, 344-347.
40. A. S. Zimmermann, B. B. Van Aken, H. Schmid, J. P. Rivera, J. Li, D. Vaknin and M. Fiebig, *The European Physical Journal B*, 2009, **71**, 355-360.
41. V. A. Streltsov, E. L. Belokoneva, V. G. Tsirelson and N. K. Hansen, *Acta Crystallogr. Sect. B*, 1993, **49**, 147-153.
42. A. Scaramucci, E. Bousquet, M. Fechner, M. Mostovoy and N. A. Spaldin, *Phys. Rev. Lett.*, 2012, **109**, 197203.
43. K. T. Delaney, E. Bousquet and N. A. Spaldin, *arXiv preprint arXiv:0912.1335*, 2009.
44. V. M. Dubovik and V. V. Tugushev, *Phys. Rep.*, 1990, **187**, 145-202.
45. B. B. Van Aken, J.-P. Rivera, H. Schmid and M. Fiebig, *Nature*, 2007, **449**, 702-705.
46. J. M. Mays, *Phys. Rev.*, 1963, **131**, 38-53.
47. A. Yamada, M. Hosoya, S.-C. Chung, Y. Kudo, K. Hinokuma, K.-Y. Liu and Y. Nishi, *J. Power Sources*, 2003, **119–121**, 232-238.
48. P. E. Blöchl, *Phys. Rev. B*, 1994, **50**, 17953-17979.
49. G. Kresse and J. Furthmüller, *Phys. Rev. B*, 1996, **54**, 11169-11186.
50. G. Kresse and J. Hafner, *Phys. Rev. B*, 1993, **47**, 558-561.
51. J. P. Perdew, A. Ruzsinszky, G. I. Csonka, O. A. Vydrov, G. E. Scuseria, L. A. Constantin, X. Zhou and K. Burke, *Phys. Rev. Lett.*, 2008, **100**, 136406.
52. F. Zhou, M. Cococcioni, C. A. Marianetti, D. Morgan and G. Ceder, *Phys. Rev. B*, 2004, **70**, 235121.
53. H. J. Monkhorst and J. D. Pack, *Phys. Rev. B*, 1976, **13**, 5188-5192.
54. D. Hobbs, G. Kresse and J. Hafner, *Phys. Rev. B*, 2000, **62**, 11556-11570.
55. M. Marsman and J. Hafner, *Phys. Rev. B*, 2002, **66**, 224409.
56. R. M. Martin, *Electronic Structure: Basic Theory and Practical Methods*, Cambridge University Press, 2004.
57. A. A. Mostofi, J. R. Yates, Y.-S. Lee, I. Souza, D. Vanderbilt and N. Marzari, *Comput. Phys. Commun.*, 2008, **178**, 685-699.
58. I. Bilecka, A. Hintennach, I. Djerdj, P. Novak and M. Niederberger, *J. Mater. Chem.*, 2009, **19**, 5125-5128.
59. R. J. Radwanski and Z. Ropka, *Physica B*, 2004, **345**, 107-110.
60. S. H. Baek, R. Klingeler, C. Neef, C. Koo, B. Büchner and H. J. Grafe, *Phys. Rev. B*, 2014, **89**, 134424.
61. J. G. Creer and G. J. Troup, *Phys. Lett. A*, 1970, **32**, 439-440.
62. J. Li, V. O. Garlea, J. L. Zarestky and D. Vaknin, *Phys. Rev. B*, 2006, **73**, 024410.
63. E. Bousquet and N. Spaldin, *Phys. Rev. B*, 2010, **82**, 220402.
64. C. Kittel, *Phys. Rev.*, 1949, **76**, 743-748.
65. L. Pauling, *J. Am. Chem. Soc.*, 1931, **53**, 1367-1400.
66. J. B. Goodenough, *Phys. Rev.*, 1968, **171**, 466-479.
67. F. S. Ham, *Phys. Rev.*, 1965, **138**, A1727-A1740.

68. J. Okamoto, H. Nakao, Y. Yamasaki, H. Wadati, A. Tanaka, M. Kubota, K. Horigane, Y. Murakami and K. Yamada, *J. Phys. Soc. Jpn.*, 2014, **83**, 044705.
69. M. S. a. I. S. Suzuki, *Department of Physics, State University of New York at Binghamton*

70. J. Kübler, *Theory of itinerant electron magnetism*, Oxford Univ. Press, 2000.
71. K. Yamauchi and S. Picozzi, *Phys. Rev. B*, 2010, **81**, 024110.
72. Y.-J. Song, K.-H. Ahn, K.-W. Lee and W. E. Pickett, *arXiv preprint arXiv:1408.4078*, 2014.
73. H. Raebiger, S. Lany and A. Zunger, *Nature*, 2008, **453**, 763-766.
74. J. B. Goodenough, *Phys. Rev.*, 1955, **100**, 564-573.
75. J. Kanamori, *J. Phys. Chem. Solids*, 1959, **10**, 87-98.
76. S. Salunke, V. R. Singh, A. V. Mahajan and I. Dasgupta, *J. Phys.: Condens. Matter*, 2009, **21**, 025603.
77. S. S. Salunke, M. A. H. Ahsan, R. Nath, A. V. Mahajan and I. Dasgupta, *Phys. Rev. B*, 2007, **76**, 085104.
78. J. Chakraborty and I. Dasgupta, *Phys. Rev. B*, 2012, **86**, 054434.
79. B. Koteswararao, A. V. Mahajan, F. Bert, P. Mendels, J. Chakraborty, V. Singh, I. Dasgupta, S. Rayaprol, V. Siruguri, A. Hoser and S. D. Kaushik, *J. Phys.: Condens. Matter*, 2012, **24**, 236001.

Figures Legend

Figure 1. Crystal structure of layered olivine. Each magnetic ion (Co or Fe) are surrounded by oxygen octahedra (a. Each magnetic layer is separated by two non-magnetic layers, which contain tetrahedrally coordinated P ions (i.e. PO_4), and octahedrally coordinated Li ions (LiO_6) (a). Relative energies for the various magnetic structure models obtained by PBE+U calculations (b), and relative energies along each spin quantization axis *x*, *y*, and *z* obtained by PBE+U+SOC calculations (c) for $LiCo_{1-x}Fe_xPO_4$ (x = 0.00, 0.25, 0.50, 0.75, and 1.00). The colored boxes contain an exhaustive set of the possible substitution of Fe ions in the LCP unit cell shown in the inset of Figure (c).

Figure 2. (a-b) displays the morphology for $LiCo_{0.25}Fe_{0.75}PO_4$, (c-d) for $LiCo_{0.5}Fe_{0.5}PO_4$ and (e-f) for $LiCo_{0.75}Fe_{0.25}PO_4$.

Figure 3. XRD Results for $LiCo_{1-x}Fe_xPO_4$, compared to the experimental pure single phases.

Figure 4. SQUID measurement of synthesized $LiCoPO_4$, $LiCo_{0.75}Fe_{0.25}PO_4$, $LiCo_{0.5}Fe_{0.5}PO_4$ and $LiCo_{0.25}Fe_{0.75}PO_4$. $\mu_0 H$ = 0.05 T , Scanning Temperature from 200 to 4 K

Figure 5. Computed spin and orbital magnetic moment direction for each magnetic ion (Co - blue sphere; Fe – brown sphere) for (b) x = 0.00, (c) x = 0.25, (d) x = 0.50, (e) x = 0.75, and (f) x = 1.00. The angle between the spin magnetic moment with the easy axis is also presented. Additionally, a schematic representation of the direction of the *L*, *S*, and *J* angular momenta for an electron, using the *L*-*S* coupling scheme, is presented in (a).

Figure 6. (a) Spin-polarized total density of states for $LiCo_{1-x}Fe_xPO_4$ for each composition, i.e. x = 0.00, 0.25, 0.50, 0.75, and 1.00, obtained by different methods (PBE, PBE+U,

PBE+SOC, and PBE+U+SOC), and (b) Plots of Co-3d (t_{2g} and e_g) and Fe-3d (t_{2g} and e_g) density of states for LCP, LFP, and for the mixed systems (using PBE+U calculations). Additionally, a schematic diagram of the expected crystal field splitting of Co^{2+} and Fe^{2+} in the high spin states is presented.

Figure 7. Calculated (a) average spin magnetic moment, (b) average orbital magnetic moment per magnetic ion, and (c) average effective magnetic moment (μ_{eff}) for each x in $LiCo_{1-x}Fe_xPO_4$. In the inset of Figure 7 (b), the value of the orbital moment corresponds to the Co and Fe magnetic ions.

Figure 8. Calculated spin-orbit coupling energy, i.e. $E_{soc,}$ for Co (a), and Fe (b) ions along the spin magnetization directions, i.e. [100], [010], [001], [011], and [111]. The most probable energy, i.e. <E>, of the orbitals of Co (c) and Fe (d) ions in $LiCo_{1-x}Fe_xPO_4$ (x = 0.00, 0.25, 0.50, 0.75, and 1.00) olivines in the valence region of the DOS.

Figure 9. Computed orbital occupancy (a) Co-3d up, (b) Co-3d down, (c) Fe-3d up, and (d) Fe-3d down, for each Co-3d and Fe-3d atomic orbitals (x^2-y^2, xy, xz, yz, and $3z^2$-r^2) for both spin channels in $LiCo_{1-x}Fe_xPO_4$ (x = 0.00, 0.25, 0.50, 0.75, and 1.00).

Figure 10. (a) Spreading of the Fe $3d_{z^2-r^2}$ Wannier function. (b) Fe $3d_{z^2-r^2}$ Wannier function for the mixed composite x = 0.25, and (c) for pure LFP i.e. x = 1.00.

Table Legends

Table 1. Summary of the effective magnetic moment (μ_{eff}) obtained experimentally, theoretically, and computationally considering, only spin (s), both orbital (l) and spin (s) moments, and J where $J = L + S$, for all x in $LiCo_{1-x}Fe_xPO_4$. Additionally, the value of modified Landé g factor and Néel temperature (T_N) as a function of x in $LiCo_{1-x}Fe_xPO_4$ (x = 0.00, 0.25, 0.50, and 1.00) are shown.

Figure 1

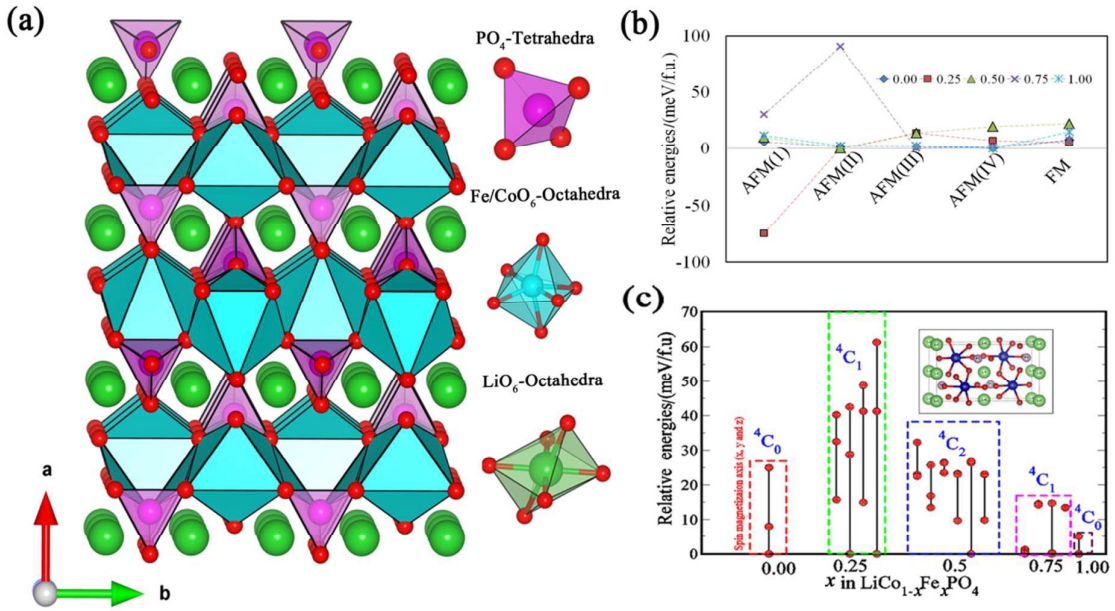

Figure 2

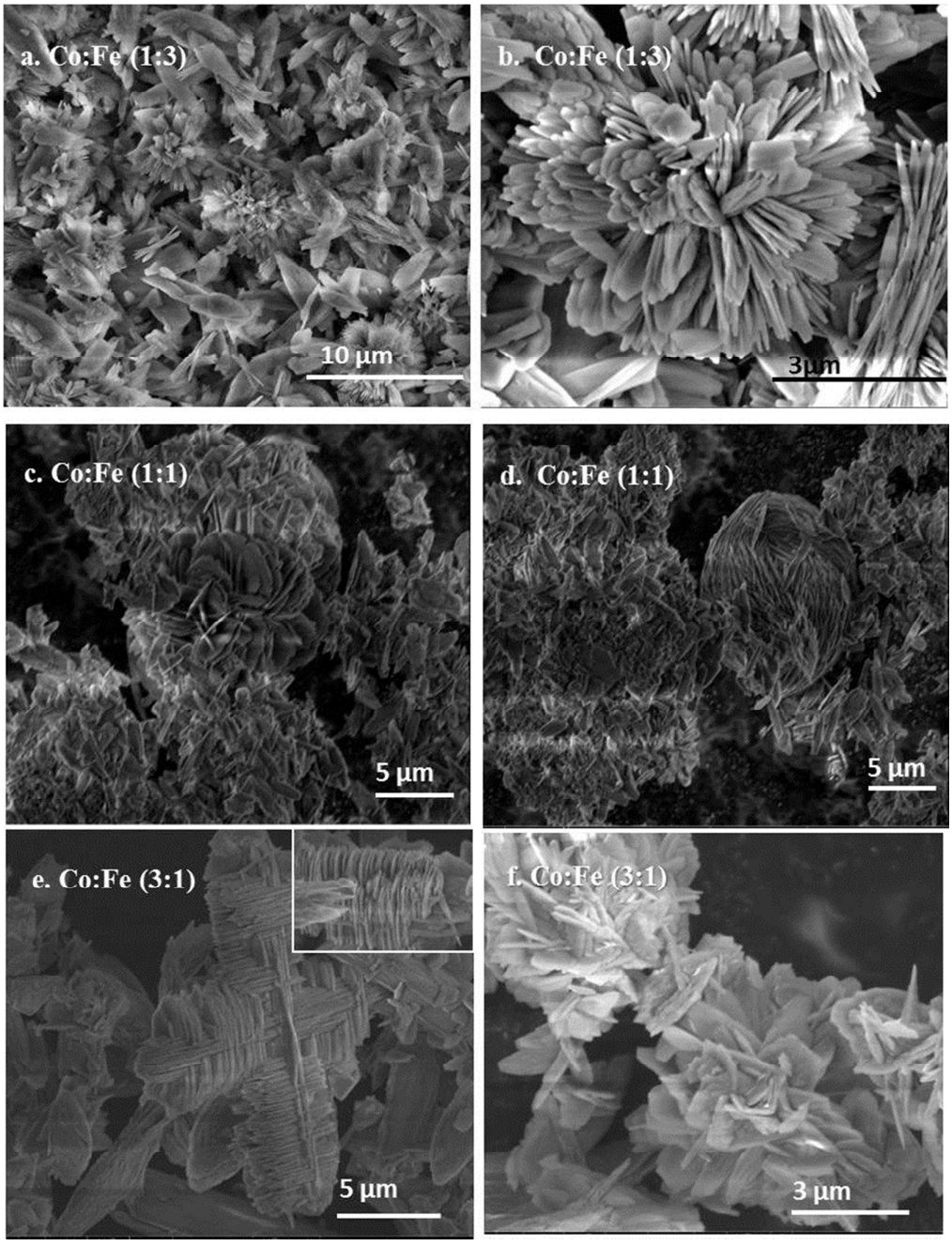

Figure 3

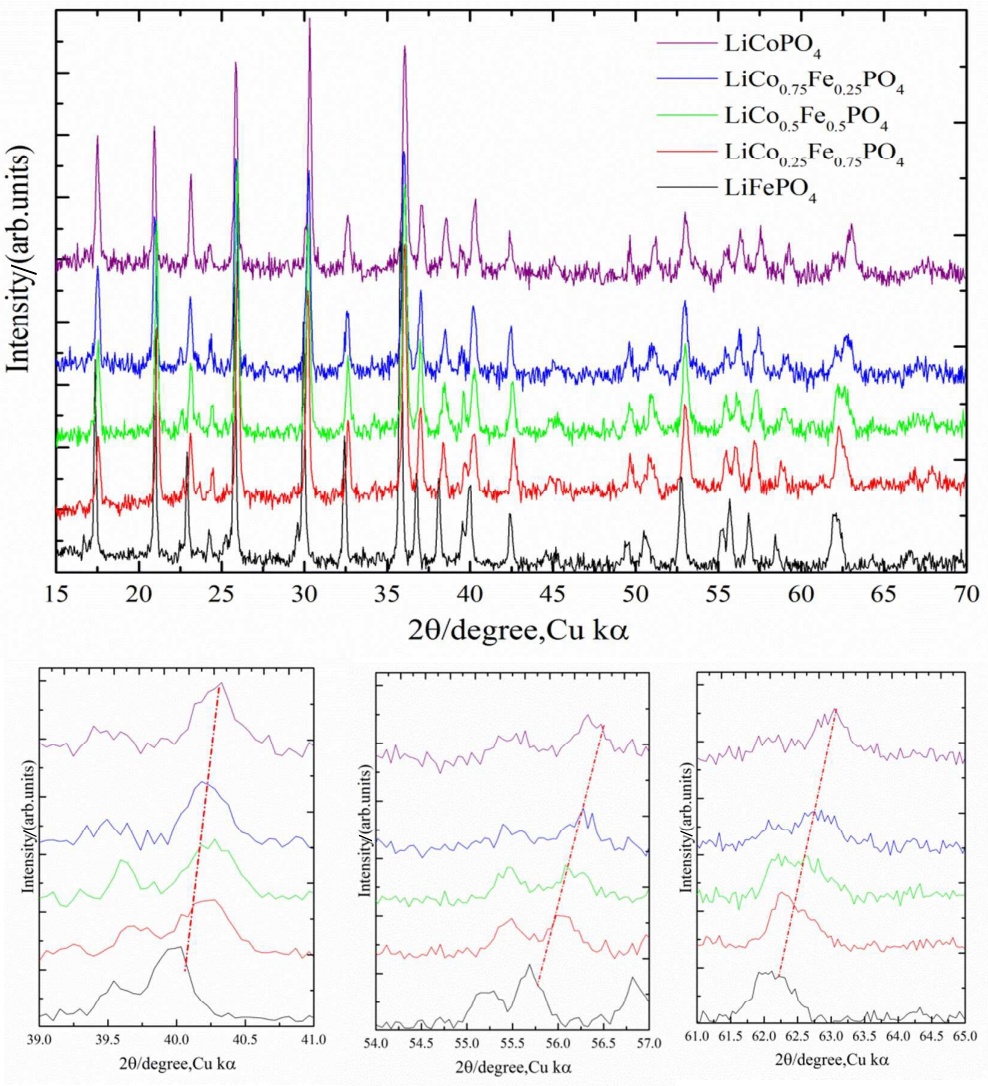

Figure 4

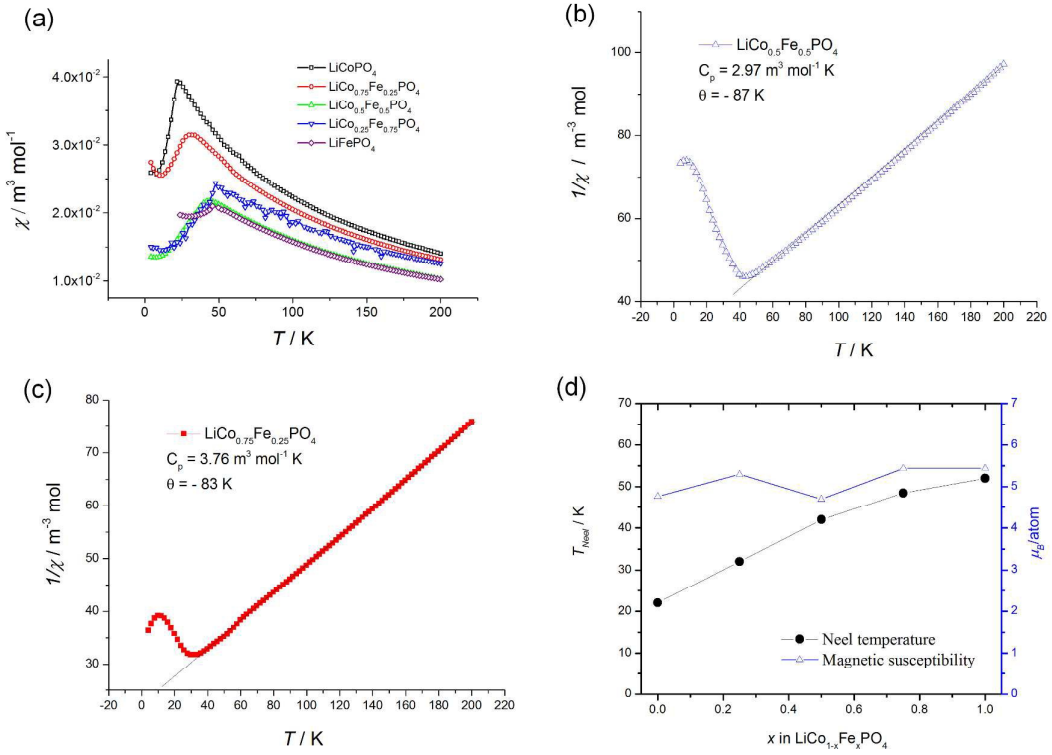

Figure 5

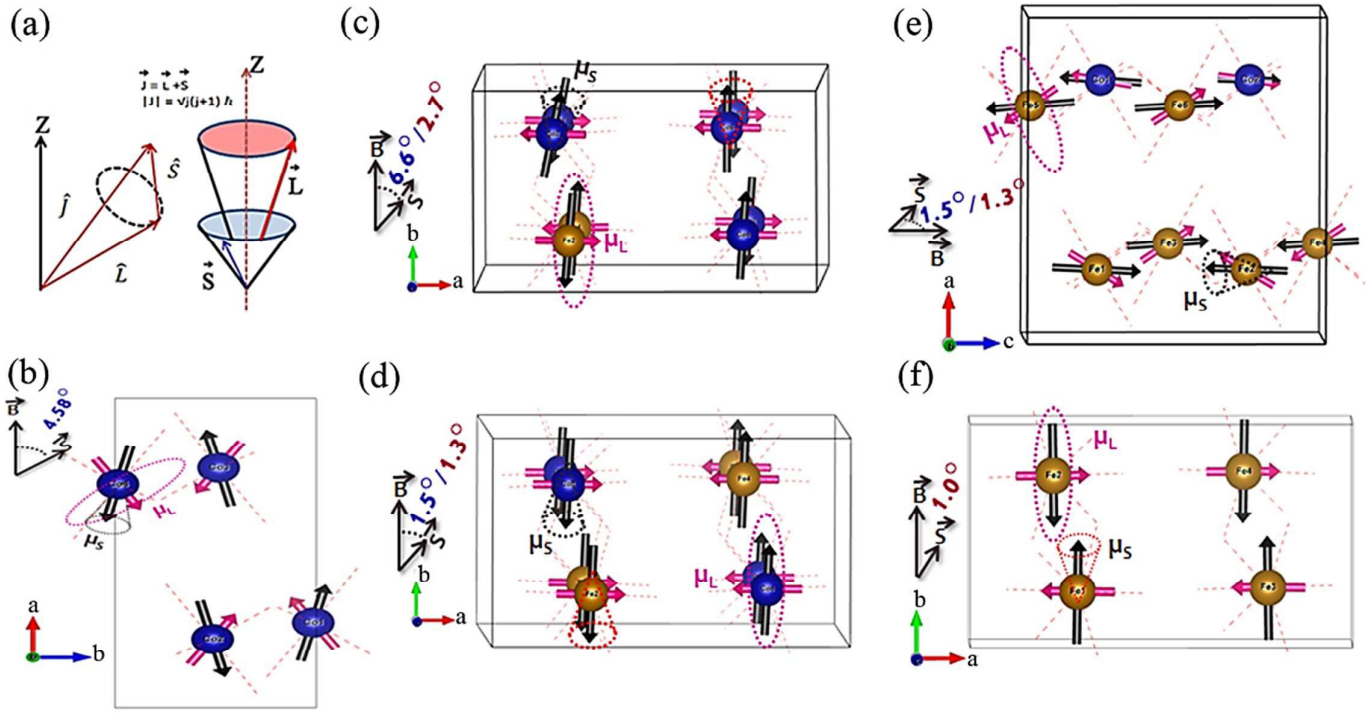

Figure 6

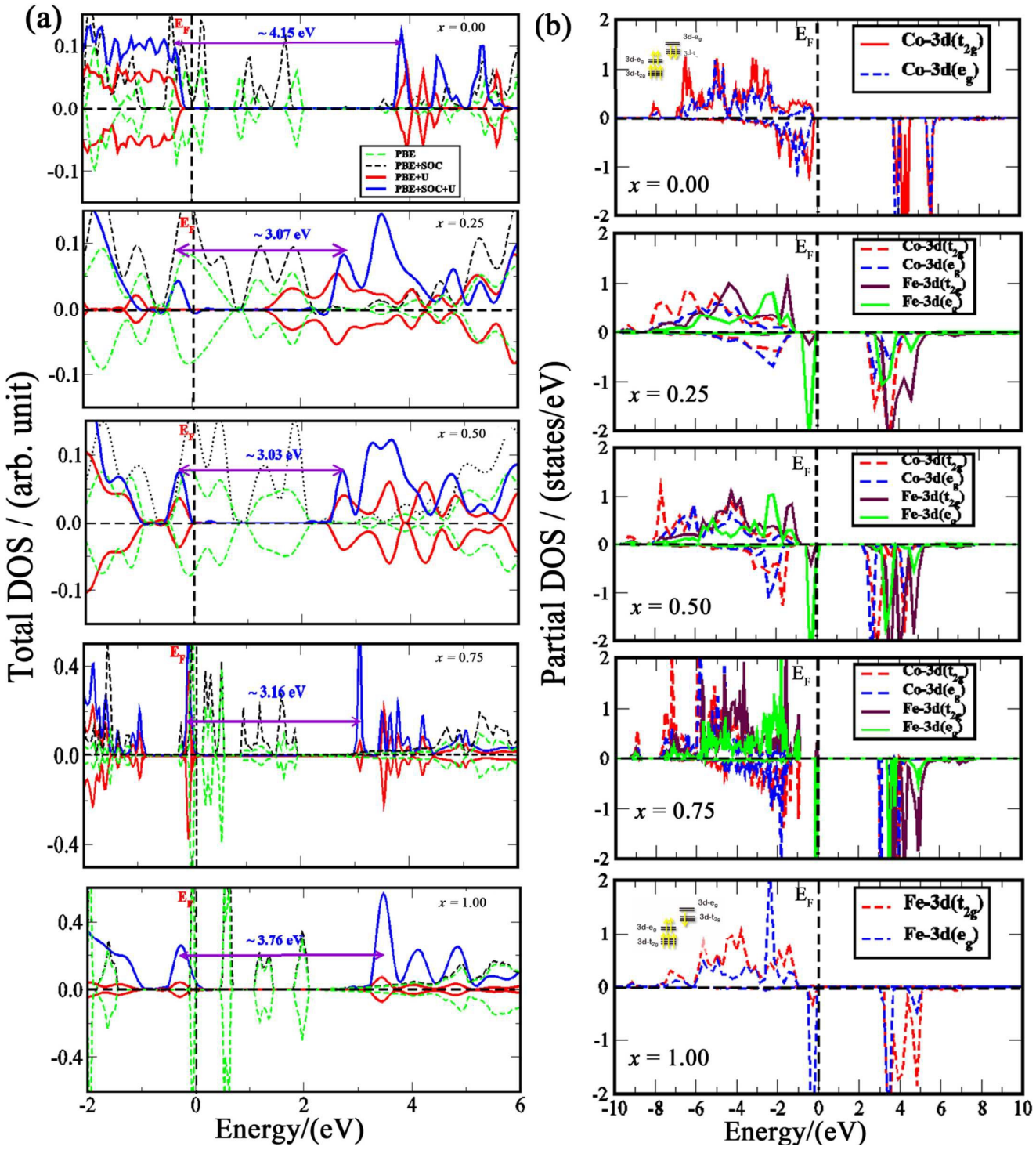

Figure 7

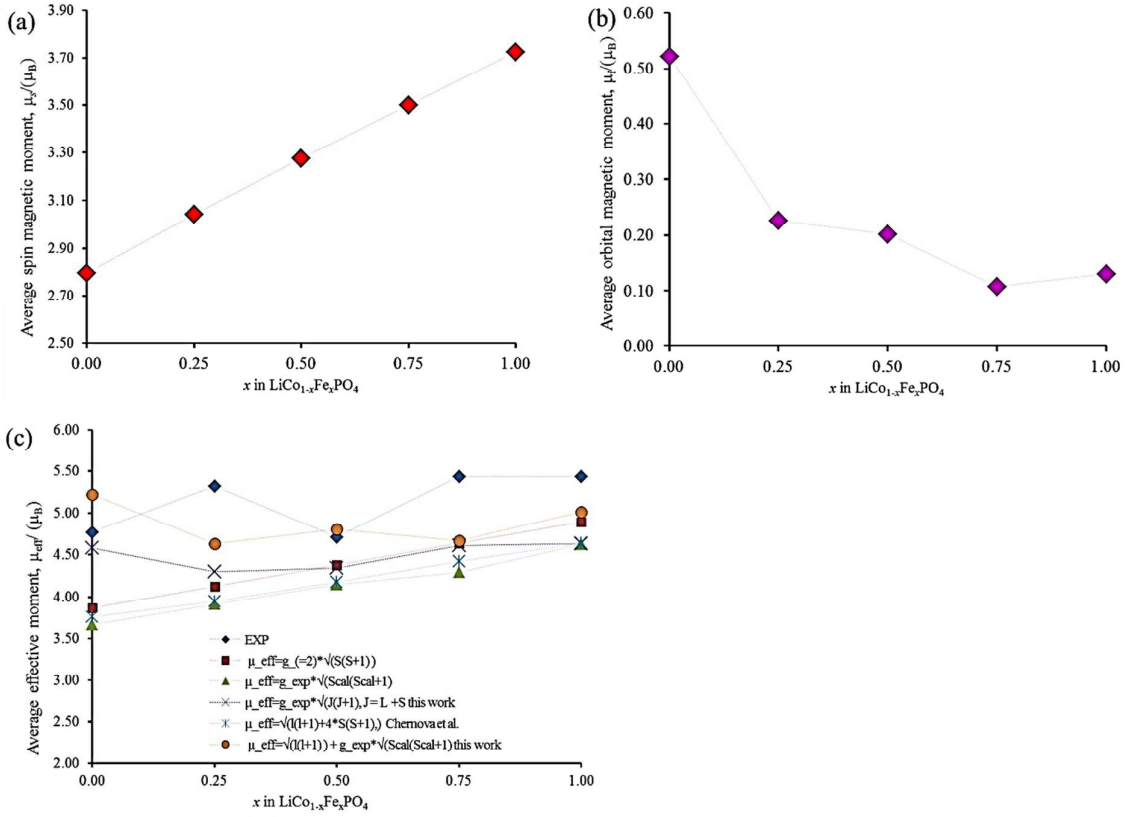

Figure 8

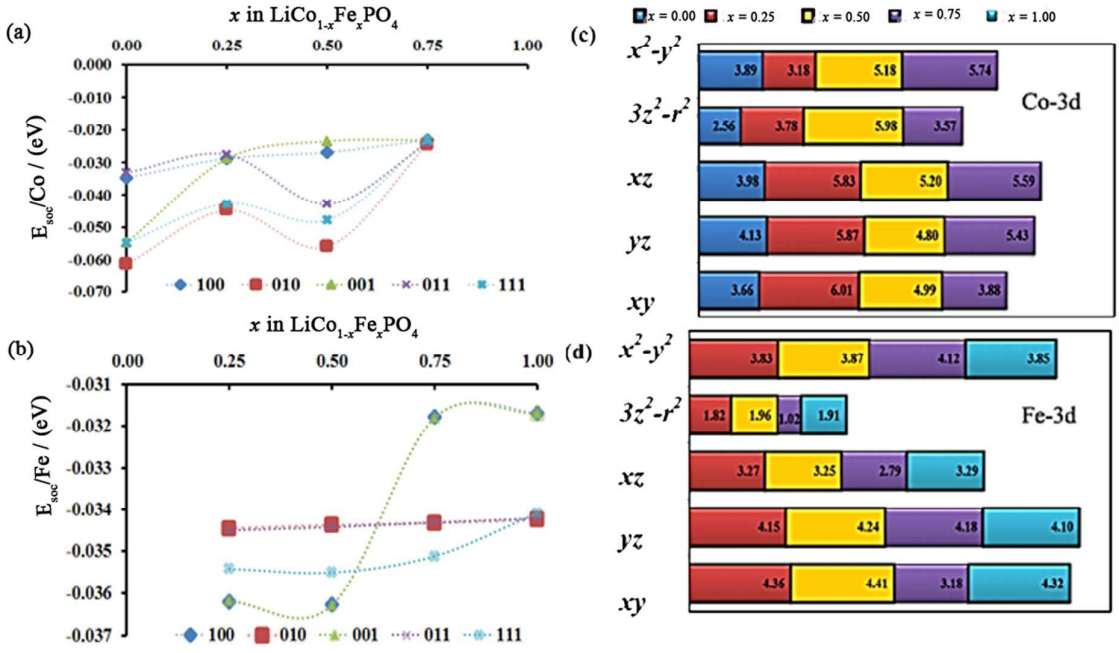

Figure 9

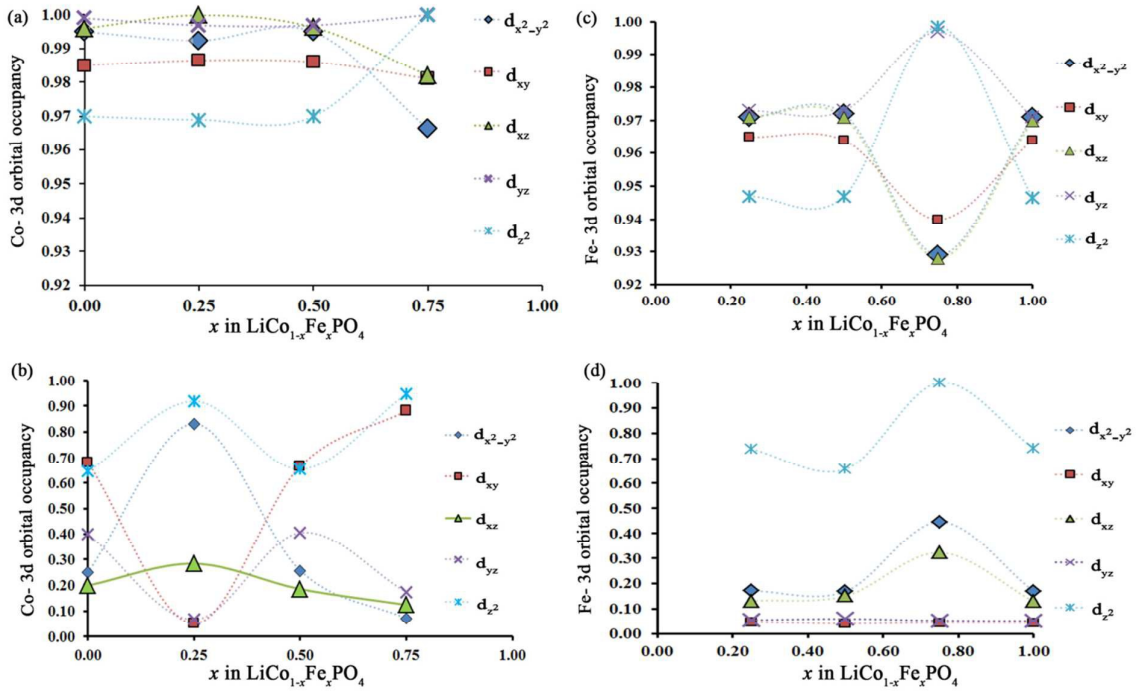

Figure (10)

Mechanism: M – O – P - O - M

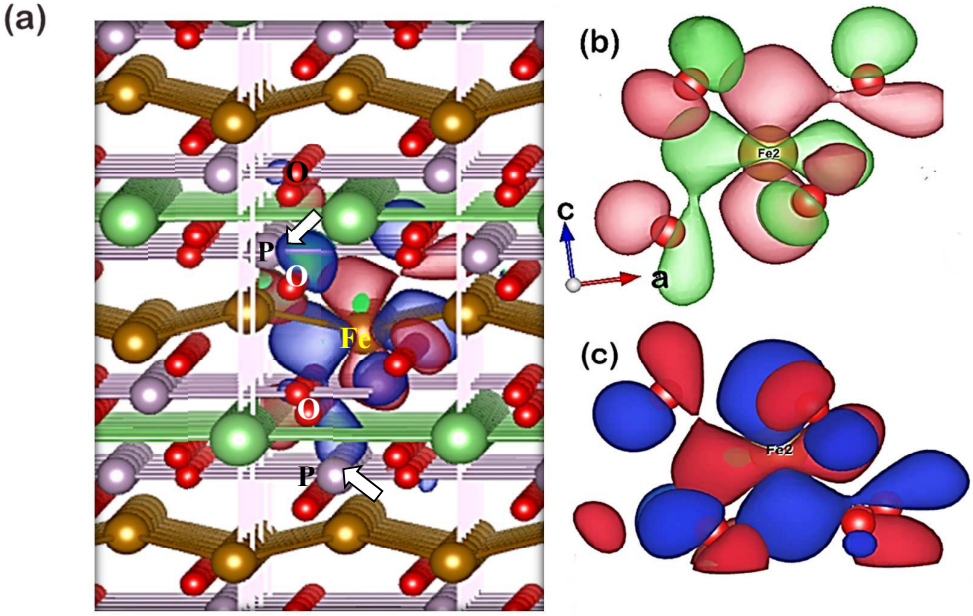

TOC

This work demonstrates that inclusion of spin-orbit coupling in first-principles calculations is essential to obtain qualitative agreement with the observed effective magnetic moments in $LiCo_{1-x}Fe_xPO_4$.

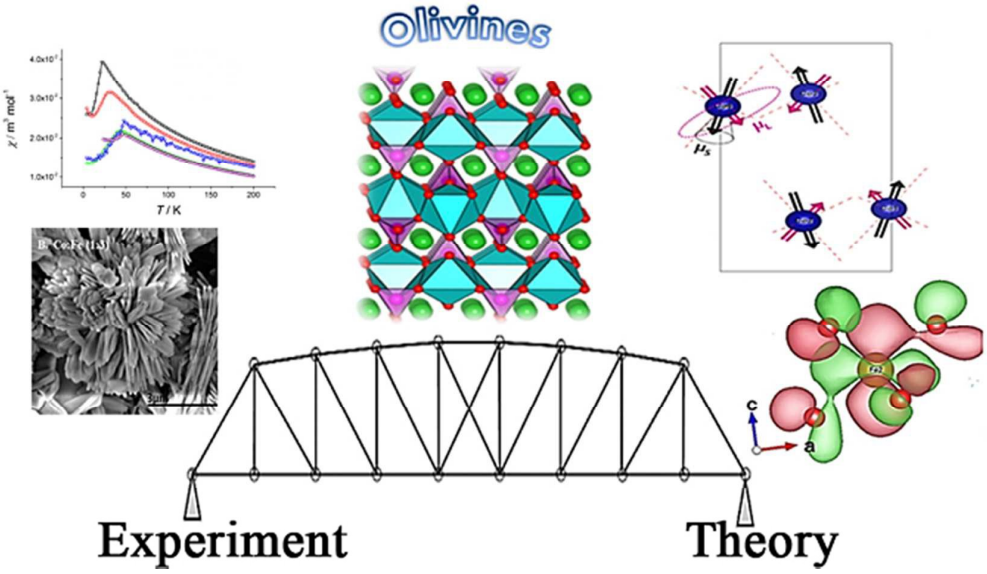

Table (I)

Compositions	Néel Temp / (°K)	g_{exp}	Effective Magnetic moment/magnetic ion (μ_{eff}) / (μ_B)						
x in $LiCo_{1-x}Fe_xPO_4$		Value /(RT)	Exp	μ_{eff} (other works)	Theory[a]	Computed[b]	Computed [c]	Computed [d]	Computed [e]
0.00	22	2.362	4.77	5.7[36], 4.62-5.28[57], 4.20[27], 5.10[59]	3.87	3.67	4.58	3.76	5.22
0.25	32	2.068	5.32		4.13	3.91	4.30	3.95	4.63
0.50	42	2.077	4.71		4.38	4.15	4.34	4.18	4.80
0.75	48.5	2.065	5.44		4.64	4.29	4.61	4.42	4.67
1.00	52	2.002	5.44	5.45[38], 6.8[37], [31], 4.95-5.43[31], 5.19-5.65[57]	4.89	4.62	4.63	4.64	5.01

a $\mu_{eff} = g_{=2} * \sqrt{S_{theo}(S_{theo}+1)}$, using spin only where $S = 3/2$ for Co^{2+} and 4/2 for Fe^{2+}

b $\mu_{eff} = g_{exp} * \sqrt{S_{cal}(S_{cal}+1)}$, using computed spin

c $\mu_{eff} = g_{exp} * \sqrt{J(J+1)}$, using both orbital and spin moments add-up to $J = L + S$

d $\mu_{eff} = \sqrt{l(l+1)+4*S(S+1)}$, using Chernova et al.[34]

e $\mu_{eff} = \sqrt{l(l+1)} + g_{exp} * \sqrt{S_{cal}(S_{cal}+1)}$, using both orbital ($\mu_l$) and spin moments ($\mu_s$)